

Article

EUV/VUV Spectroscopy for the Study of Carbon Impurity Transport in Hydrogen and Deuterium Plasmas in the Edge Stochastic Magnetic Field Layer of Large Helical Device

Tetsutarou Oishi ^{1,*}, Shigeru Morita ^{2,3}, Masahiro Kobayashi ^{2,3}, Gakushi Kawamura ^{2,3}, Yasuko Kawamoto ^{2,3}, Tomoko Kawate ^{2,3}, Suguru Masuzaki ^{2,3}, Chihiro Suzuki ^{2,3} and Motoshi Goto ^{2,3}

¹ Department of Quantum Science and Energy Engineering, Tohoku University, 6-6-01-2 Aobayama, Sendai 980-8579, Japan

² National Institute for Fusion Science, National Institutes of Natural Sciences, 322-6 Oroshi-cho, Toki 509-5292, Japan; morita@nifs.ac.jp (S.M.); kobayashi.masahiro@nifs.ac.jp (M.K.); kawamura.gakushi@nifs.ac.jp (G.K.); kawamoto.yasuko@nifs.ac.jp (Y.K.); kawate.tomoko@nifs.ac.jp (T.K.); masuzaki.suguru@nifs.ac.jp (S.M.); suzuki.chihiro@nifs.ac.jp (C.S.); goto@nifs.ac.jp (M.G.)

³ Department of Fusion Science, The Graduate University for Advanced Studies, SOKENDAI, 322-6 Oroshi-cho, Toki 509-5292, Japan

* Correspondence: tetsutarou.oishi.a4@tohoku.ac.jp

Citation: Oishi, T.; Morita, S.; Kobayashi, M.; Kawamura, G.; Kawamoto, Y.; Kawate, T.; Masuzaki, S.; Suzuki, C.; Goto, M. EUV/VUV Spectroscopy for the Study of Carbon Impurity Transport in Hydrogen and Deuterium Plasmas in the Edge Stochastic Magnetic Field Layer of Large Helical Device. *Plasma* **2023**, *6*, 308–321. <https://doi.org/10.3390/plasma6020021>

Academic Editor: Andrey Starikovskiy

Received: 15 March 2023

Revised: 10 May 2023

Accepted: 11 May 2023

Published: 12 May 2023



Copyright: © 2023 by the authors. Licensee MDPI, Basel, Switzerland. This article is an open access article distributed under the terms and conditions of the Creative Commons Attribution (CC BY) license (<https://creativecommons.org/licenses/by/4.0/>).

Abstract: The ergodic layer in the Large Helical Device (LHD) consists of stochastic magnetic fields exhibiting a three-dimensional structure that is intrinsically formed by helical coils. Spectroscopic diagnostics was employed in the extreme ultraviolet (EUV) and vacuum ultraviolet (VUV) wavelength ranges to investigate emission lines of carbon impurities in both hydrogen (H) and deuterium (D) plasmas, aiming to elucidate the impact of distinct bulk ions on impurity generation and transport in the edge plasmas of the LHD. The emission intensity of carbon CIII, CIV, CV, and CVI lines is significantly higher in the D plasma compared to the H plasma, indicating a greater sputtering rate of carbon materials in the D plasma, resulting in a higher quantity of carbon impurities originating from the divertor plates. A Doppler profile measurement of the second order of CIV line emission ($1548.20 \times 2 \text{ \AA}$) was attempted using a 3 m normal-incidence VUV spectrometer in the edge plasma at a horizontally elongated plasma position. The flow velocity reaches its maximum value close to the outermost region of the ergodic layer, and the observed flow direction aligns with the friction force in the parallel momentum balance. The flow velocity increases with the electron density in H plasmas, suggesting that the friction force becomes more dominant in the force balance at higher density regimes. This leads to an increase in the impurity flow, which can contribute to the impurity screening. In contrast, the flow velocity in the D plasma is smaller than that in the H plasma. The difference in flow values between D and H plasmas, when the friction force term dominates in the momentum balance, could be attributed to the mass dependence of the thermal velocity of the bulk ions.

Keywords: space-resolved spectroscopy; extreme ultraviolet; vacuum ultraviolet; magnetically confined fusion; impurity transport; stochastic magnetic field

1. Introduction

In the domain of magnetically confined fusion plasmas, the term “edge plasma” denotes a region characterized by open magnetic field lines enveloping the core plasmas. Within this region, impurity ions originating from the plasma-facing components can penetrate the plasma, potentially leading to plasma contamination and cooling. Consequently, controlling the processes associated with impurity generation and transport is a pivotal factor for achieving steady-state operation and high performance in fusion

reactors. To gain insight into impurity behavior in the edge plasmas, numerous endeavors have been made to investigate the effects of edge magnetic field stochasticization on plasma detachment and impurity transport [1–3]. In the Large Helical Device (LHD), magnetic flux surfaces are well-defined up to the last closed flux surface (LCFS). However, at the edge, a thick region of stochastic magnetic field with a three-dimensional structure, referred to as the “ergodic layer,” is intrinsically formed by the helical coils [4]. Therefore, examining impurity behavior and transport within the ergodic layer and comparing it to the behavior in the tokamak scrape-off layer provides valuable insights into impurity control in the edge plasmas. Carbon serves as the most abundant impurity within the edge plasma of LHD, originating from the carbon divertor plates. It has been discovered that the presence of the ergodic layer results in the screening of carbon impurities [5], with even more effective screening of iron impurities. Consequently, the iron density in LHD core plasmas remains remarkably low, despite the vacuum vessel being constructed from stainless steel [6]. The phenomenon of “impurity screening” has also been compared between the scrape-off layer of a tokamak and the ergodic layer of a helical device [7].

Accurate characterization of impurity behavior is of utmost significance in comprehending impurity transport within the edge ergodic layer. A transport model has been proposed to elucidate impurity behavior in the ergodic layer, predicated on parallel momentum balance experienced by impurity ions along a magnetic field line that connects the core plasma and the divertor plate. This balance is described by the following equation:

$$m_z \frac{\partial V_{z//}}{\partial t} = -\frac{1}{n_z} \frac{\partial T_z n_z}{\partial s} + ZeE_{//} + m_z \frac{V_{i//} - V_{z//}^{imp}}{\tau_s} + 0.71Z^2 \frac{\partial T_e}{\partial s} + 2.6Z^2 \frac{\partial T_i}{\partial s} \quad (1)$$

where s denotes the coordinate along the magnetic field. The terms on the right-hand side represent contributions of impurity ion pressure gradient, parallel electric field, friction force between bulk ions and impurity ions, electron thermal force, and ion thermal force, respectively, in that particular order [8]. Among these terms, the dominant ones are the friction force and the ion thermal force. An augmentation in the ion density gradient leads to an escalation in friction force, consequently directing the impurity flow towards the divertor plates and resulting in impurity screening. Conversely, an increase in the ion temperature gradient leads to a rise in the ion thermal force, thereby directing the impurity flow towards the core plasmas and causing impurity penetration. Precise measurements of impurity flow profiles hold vital importance in examining the validity of theoretical models concerning impurity transport within stochastic magnetic field layers. Recently, carbon flow within the ergodic layer was measured in hydrogen (H) plasmas using vacuum ultraviolet (VUV) spectroscopy. Significantly, the relationship between impurity flow and impurity screening was experimentally confirmed for the first time through a comparative analysis of spectroscopic observations with impurity transport simulations based on three-dimensional simulation code known as EMC3-EIRENE [9–11].

One of the subsequent critical steps involves elucidating the impact of isotope effects of bulk ions on impurity transport, with the aim of anticipating impurity behavior in deuterium (D)–tritium (T) mixture plasmas in forthcoming fusion devices. In accordance with the aforementioned theoretical model, the frictional force responsible for impurity screening arises from collisions between bulk ions and impurity ions. Therefore, variations in the mass of bulk ions may also influence the screening effect. Consequently, the present study employed spectroscopic diagnostics for carbon impurities in both hydrogen and deuterium plasmas, aiming to clarify the influence of bulk ion mass on impurity transport within the ergodic layer.

2. Spectroscopic Diagnostics for Impurity Ions in the Edge Plasmas of LHD

The LHD is a superconducting device designed to confine plasma utilizing a heli-
tron magnetic configuration [12]. In its standard configuration, the plasma possesses major and minor radii of 3.6 m and 0.64 m, respectively. The coil system consists of 2

continuous superconducting helical coils with a poloidal pitch number of 2 and a toroidal pitch number of 10, along with 3 pairs of superconducting poloidal coils. From March 2017 to December 2022, plasma experiments employing deuterium as the operating gas were conducted at the LHD, with extensive comparisons to experiments utilizing hydrogen plasma [13]. Figure 1 illustrates schematic drawings of toroidal plasma with helical coils, as well as a horizontally elongated poloidal cross-section of the LHD. In the torus coordinate system, the coordinates R and z represent the major radial coordinate and the vertical coordinate, respectively. Poincaré plots of the stochastic magnetic fields within the ergodic layer under vacuum conditions are displayed for the poloidal cross-section corresponding to the position of the magnetic axis, R_{ax} , of 3.6 m. The stochastic magnetic fields within the edge ergodic layer are depicted with a color scale indicating the magnetic field connection length, along with the magnetic surfaces. The ergodic layer primarily consists of stochastic magnetic field lines with connection lengths ranging from 10 to 2000 m, corresponding to 0.5–100 toroidal turns in the LHD. The radial thickness of the ergodic layer exhibits variations in both toroidal and poloidal directions. When the magnetic axis is shifted outward, the ergodic layer becomes wider, resulting in a smaller plasma size within the LCFS.

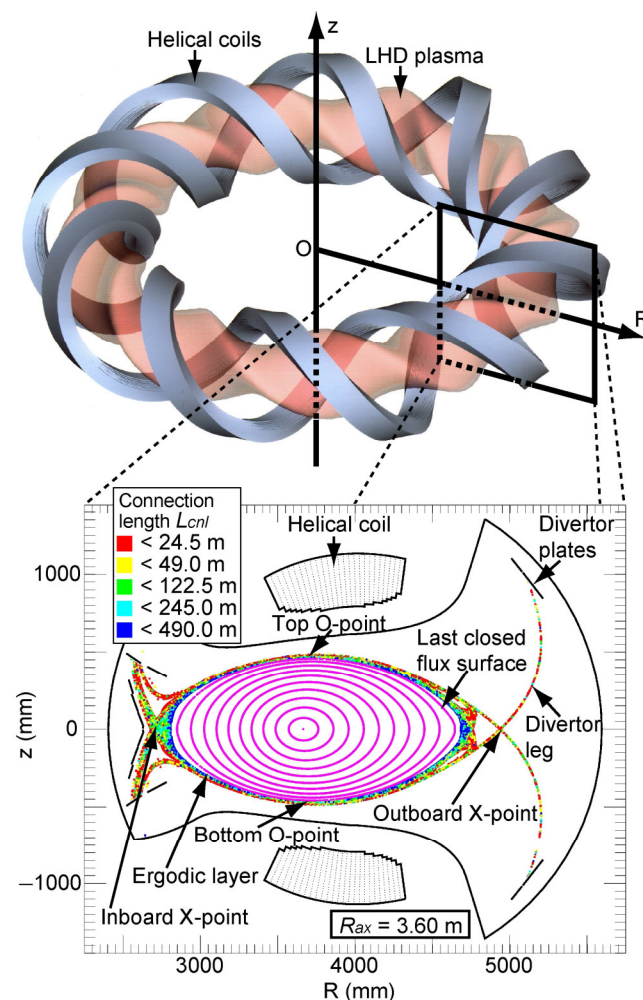


Figure 1. Schematic drawings of toroidal plasma with helical coils, as well as a horizontally elongated poloidal cross-section of the LHD. In the torus coordinate system, the coordinates R and z represent the major radial coordinate and the vertical coordinate, respectively. Poincaré plots of the stochastic magnetic fields within the ergodic layer under vacuum conditions are displayed for the poloidal cross-section corresponding to the position of the magnetic axis, R_{ax} , of 3.6 m.

The spectroscopic diagnostics in the LHD involves the utilization of several specialized instruments, including two flat-field grazing incidence EUV spectrometers referred to as “EUV Short” [14] and “EUV Long” [15], three 20 cm normal-incidence VUV spectrometers named “VUV 109L”, “VUV 106R”, and “VUV 102R” [16], and a 3 m normal-incidence VUV spectrometer known as “VUV 3m” [17]. Figure 2 provides an illustration, with Figure 2a offering a top view of the optical axes of the spectrometers and the vacuum magnetic surfaces corresponding to R_{ax} of 3.6 m. These specialized diagnostic instruments are positioned at an outer port of the LHD, referred to as “10-O”. Two types of spectroscopic measurements are conducted, as described below.

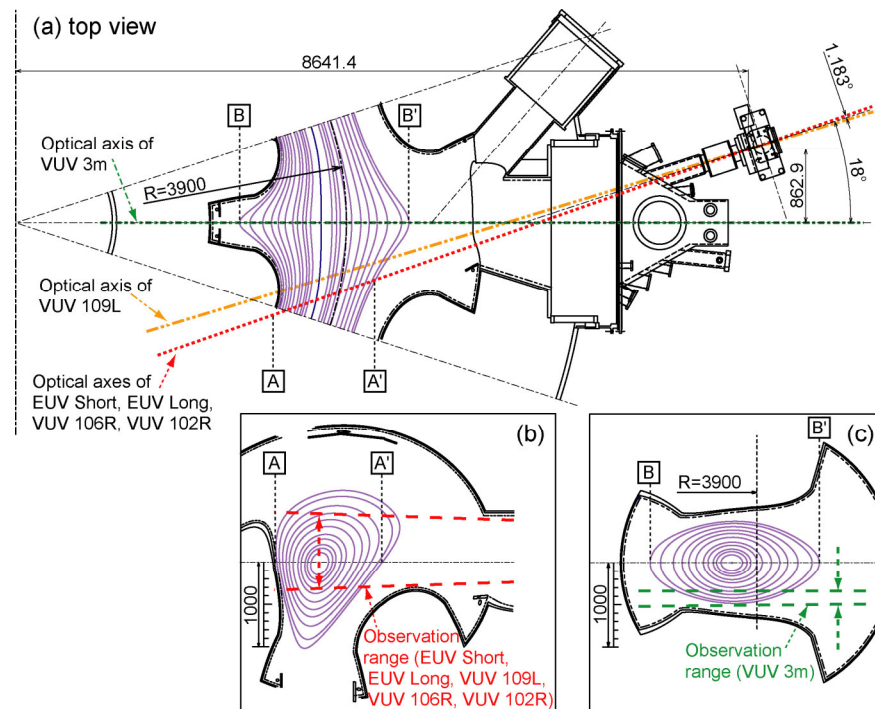


Figure 2. Observation geometry of EUV and VUV spectroscopy diagnostics in LHD. (a) Top view of optical axes of two grazing incidence flat-field EUV spectrometers (“EUV Short” and “EUV Long”), three normal-incidence 20 cm VUV spectrometers (“VUV 109L”, “VUV 106R”, and “VUV 102R”), and a space-resolved normal-incidence 3 m VUV spectrometer (“VUV 3m”) depicted together with magnetic surfaces ($R_{ax} = 3.6$ m). Plasma cross-section including the vertical observation range of (b) EUV Short, EUV Long, VUV 109L, VUV 106R, and VUV 102R and (c) VUV 3m. A, A', B, and B' in the subfigures represent the positions of the LCFS on the midplane in each plasma cross-section, respectively.

- (1) High-time-resolution EUV and VUV wavelength spectral measurements: The spectrometers EUV Short, EUV Long, VUV 109L, VUV 106R, and VUV 102 cover specific wavelength ranges of 5–60 Å, 75–260 Å, 300–1050 Å, 970–1870 Å, and 1510–2400 Å, respectively. Figure 2b illustrates the vertical observation range on a plasma cross-section, including the optical axes of these spectrometers. CCD detectors (1024 × 256 pixels, pixel size 26 μm × 26 μm, Andor DO420-BN) are positioned at the exit slits of the spectrometers. In this experiment, a CCD data acquisition mode called “full-binning” mode is utilized. In this mode, all CCD pixels aligned vertically are combined into a single channel, eliminating the vertical spatial resolution. The spectral measurements have a time resolution of 5 ms with the full-binning data acquisition mode. This measurement technique enables simultaneous coverage of a wide wavelength range from EUV to VUV. It has been applied to survey the emission spectra of various impurities, including neon injected by gas puffing [18], boron and nitrogen injected by powder dropping [19], and tungsten injected as pellets [20].

- (2) Profile measurements for emission intensity, ion temperature, and flow velocity with high-spectral-resolution VUV spectroscopy: A 3 m normal-incidence VUV spectrometer has been developed to measure the radial distribution of VUV lines within the wavelength range of 300–3200 Å in the edge plasmas of LHD. The spectrometer is equipped with a CCD detector (1024 × 1024 pixels, pixel size 13 μm × 13 μm, Andor DO934P-BN) positioned at the exit slits. The spectroscopic system has a high spectral resolution with a wavelength dispersion of 0.037 Å/CCD-pixel, enabling precise measurement of the Doppler profiles of impurity line spectra. The vertical observation range of this spectrometer is adjusted to cover the ergodic layer at the bottom edge of the LHD plasma, as depicted in Figure 2c. The observed region corresponds to the horizontally elongated poloidal cross-section. In the measurement, a “Multi-track” data acquisition mode is employed, where multiple pixels are binned together (known as “binning”) to reduce the signal read time. Specifically, the CCD signals are summed up every 10 vertical pixels, resulting in a single vertical channel. This allows the division of the observable region into 102 observation chords. Each profile image can be captured with a time interval of 200 ms, comprising an exposure time of 138.66 ms and a readout time of 61.34 ms. The high wavelength dispersion of the spectrometer enables detailed wavelength identification of impurity emission lines. This measurement technique has been applied to study carbon, neon, argon [21], and tungsten impurities [22], providing valuable information on their emission profiles and behavior in the plasma.

3. Spectroscopic Observation of Carbon Impurity

Figure 3 provides a typical waveform of a discharge, with a magnetic configuration characterized by $R_{ax} = 3.6$ m and a toroidal magnetic field, B_t , of 2.75 T, oriented in a counter-clockwise direction from a top-down perspective. The figure shows the time evolution of various parameters as follows: (a) the injection power of the electron cyclotron heating (ECH) and the neutral beam injection sourced from negative ion sources (n-NBI); (b) the central electron temperature, T_{e0} ; (c) the line-averaged electron density, \bar{n}_e , with a gas-puffing duration of D₂; (d) the plasma stored energy, W_p ; and (e) the emission intensity of D_α, H_α, and the neutral particle ratio of D/(H + D).

The discharge is initiated by ECH and further heated by three n-NBI beams with a total port-through power of 14 MW. Despite using deuterium as the operating gas and hydrogen as the neutral beam particle, the ratio of neutral deuterium particles reaches up to 90 percent, as shown in Figure 3e, hence the plasma is referred to as “D plasma” in this paper. Figure 3f displays the spatial profiles of electron temperature, T_e , and electron density, n_e , obtained through Thomson scattering. These profiles are acquired during the discharge indicated in Figure 3a–e at a timing of 4.2 s, corresponding to the flat-top phase. The electron temperature reaches its maximum value at the plasma center, while the electron density exhibits a hollow profile. These characteristic T_e and n_e profiles are commonly observed in the LHD. Figure 4 showcases the EUV/VUV spectra comprising intrinsic impurity line emissions. The spectral data were acquired through averaging over the interval of 4.0–4.4 s in a D plasma, as depicted in Figure 3. In the spectra, the signal data were recorded for each CCD pixel aligned in the wavelength direction; thus, the units of the vertical axes indicate that it is the emission intensity per measurement channel.

The spectral identifications in this paper rely on the NIST database [23]. Carbon is the predominant impurity species in LHD due to the utilization of carbon materials in the divertor plates. Additionally, iron from the first wall material and oxygen adhering to the inner surface of the vacuum vessel also contribute significantly to the impurity contents. It is worth noting that there are also faint lines observed from boron and argon. In LHD, boronization, a process of coating the inner walls of the vacuum vessel with boron, is performed to suppress the release of oxygen [24]. The coated boron acts as a source of boron ions, which manifest as a line spectrum. Ion temperature at the plasma center is

determined using X-ray crystal spectroscopy by analyzing the Doppler broadening of the argon ion line spectrum [25]. Even in discharges without introduced argon gas, the line spectrum of argon ions can be observed due to the presence of residual gas inside the vacuum vessel. In this study, we aimed to assess impurity screening by utilizing the resonance lines of carbon impurity ions, specifically CIII (977.03 Å, 2s²-2s2p), CIV (1548.02 Å, 2s-2p), CV (40.27 Å, 1s²-1s2p), and CVI (33.73 Å, 1s-2p), as indicators of impurity emission, and by comparing the emissions at different charge states. The ionization potentials, E_i , of C²⁺, C³⁺, C⁴⁺, and C⁵⁺ are 48 eV, 65 eV, 392 eV, and 490 eV, respectively. Therefore, CIII and CIV radiation primarily originates from carbon ions with low E_i , located in the outer region of the ergodic layer, while CV and CVI radiation is emitted by carbon ions with high E_i , situated in the inner region of the ergodic layer.

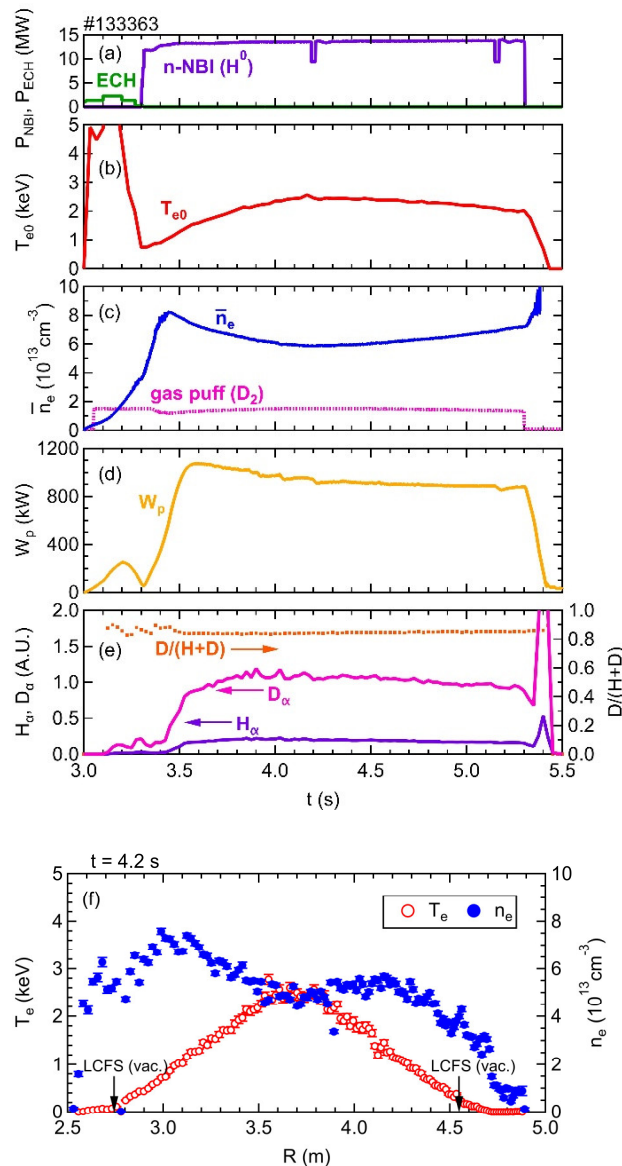


Figure 3. Typical waveform of a discharge in which the EUV/VUV spectroscopy is applied. (a) ECH and n-NBI power, (b) central electron temperature, T_{e0} , (c) line-averaged electron density, \bar{n}_e , with a waveform of the working gas puffing, (d) stored energy, (e) emission intensity of D_α, H_α, and the neutral particle ratio of D/(H + D). (f) Profiles of T_e and n_e at $t = 4.2$ s.

Figure 5 exhibits the dependence of line intensity on the line-averaged electron density for different charge states: (a) CIII, (b) CIV, (c) CV, and (d) CVI, normalized by the line-averaged electron density. The results clearly demonstrate that the emission intensity

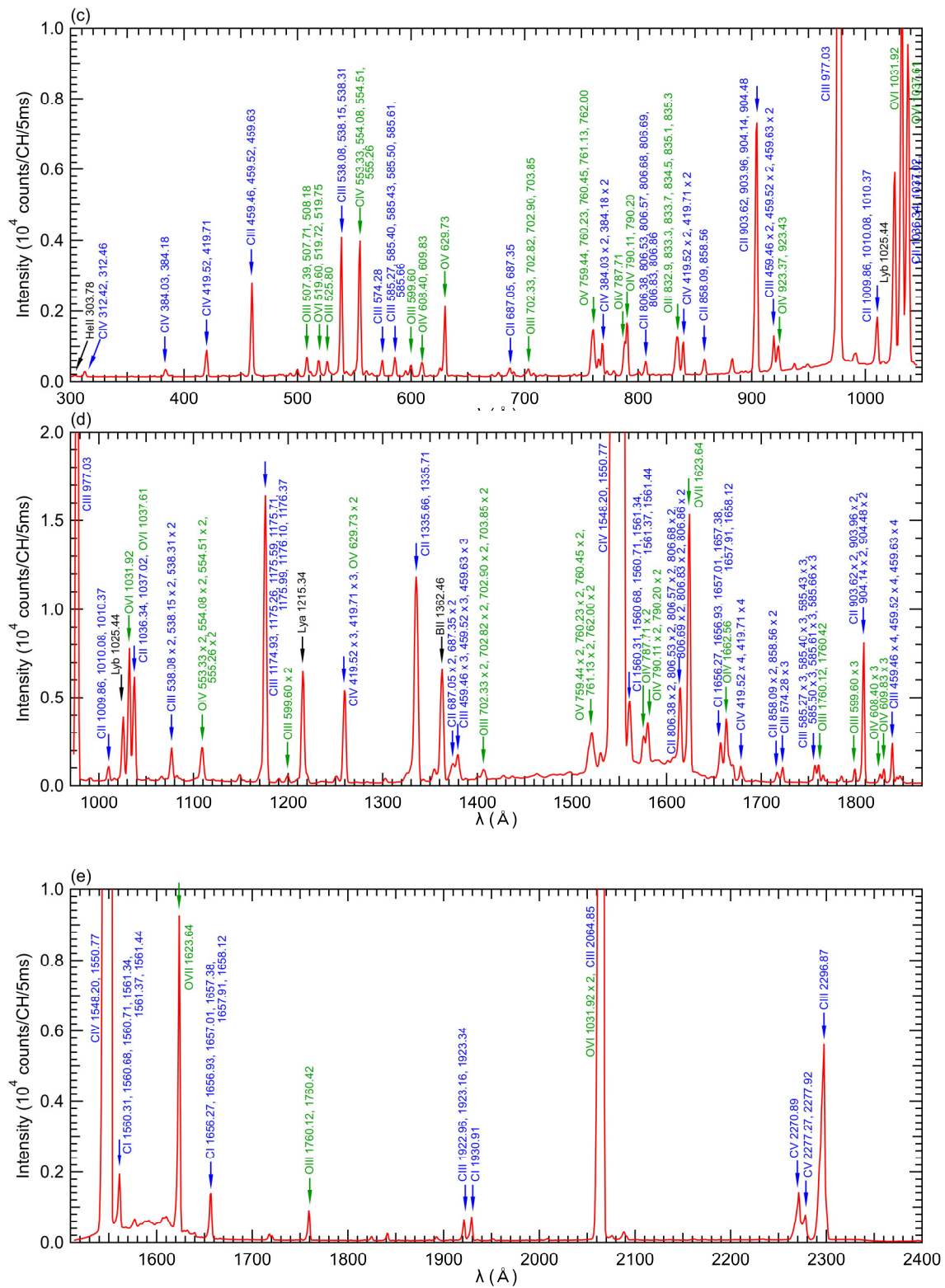


Figure 4. Typical EUV/VUV spectra in the wavelength ranges of (a) 5–60 Å measured by “EUV Short” spectrometer, (b) 75–260 Å measured by “EUV Long” spectrometer, (c) 300–1050 Å measured by “VUV 109L” spectrometer, (d) 970–1870 Å measured by “VUV 106R” spectrometer, and (e) 1510–2400 Å measured by “VUV 102R” spectrometer for a D plasma. The spectra were averaged over 4.0–4.4 s.

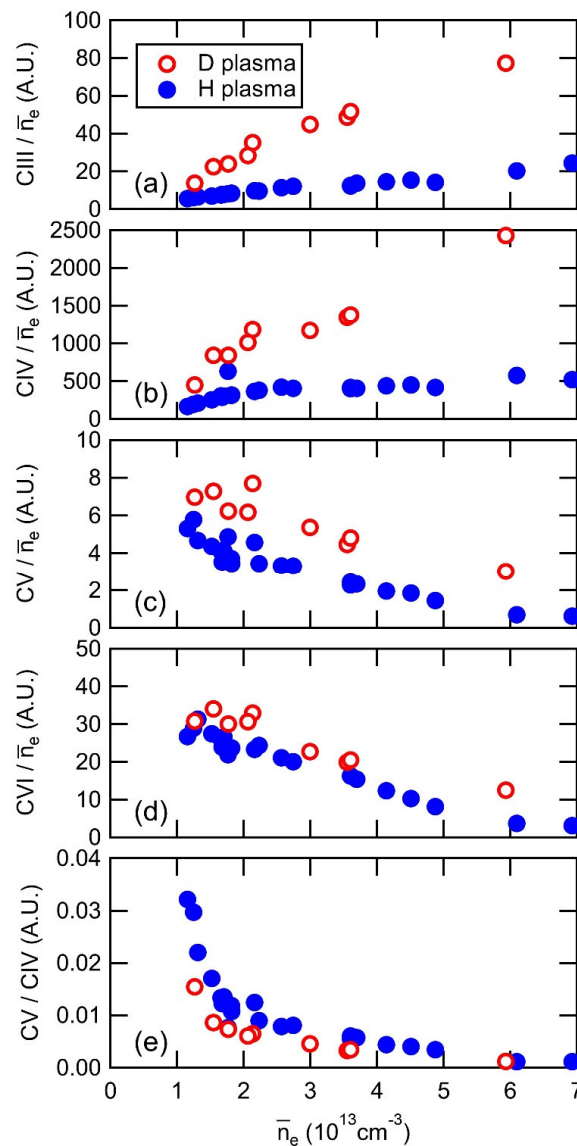


Figure 5. Line-averaged electron density dependence of line intensity of (a) CIII, (b) CIV, (c) CV, (d) CVI normalized by the electron density and (e) line ratio CV/CIV for deuterium and hydrogen discharges.

During the flat-top phase of the discharges, a space-resolved VUV spectroscopy was conducted using a 3 m normal-incidence VUV spectrometer. The measurement was specifically performed from 4.0 to 4.4 s in the discharge shown in Figure 3. The VUV spectroscopy employed the viewing angle of the edge profile measurement to achieve high spatial resolution. The Doppler shift of the second order of CIV line emission ($1548.20 \times 2 \text{ \AA}$) was utilized to investigate the spatial profiles of emission intensity, ion temperature, and flow velocity of C^{3+} ions. The measurements were focused on a horizontally elongated plasma position in LHD. Figure 6 presents the wavelength spectrum covering the entire wavelength range observed in a single discharge, including CIV lines with wavelengths of 1548.20×2 and $1550.77 \times 2 \text{ \AA}$. Some spike noises attributed to neutrons and γ -rays can be observed in the spectrum obtained for D plasmas [27]. However, the impact of these noises is not significant in the discharges analyzed in this study. Therefore, CIV line intensity, ion temperature, and flow velocity derived from the Doppler profile of the CIV line with a wavelength of $1548.20 \times 2 \text{ \AA}$ can be obtained for both H plasmas and D plasmas.

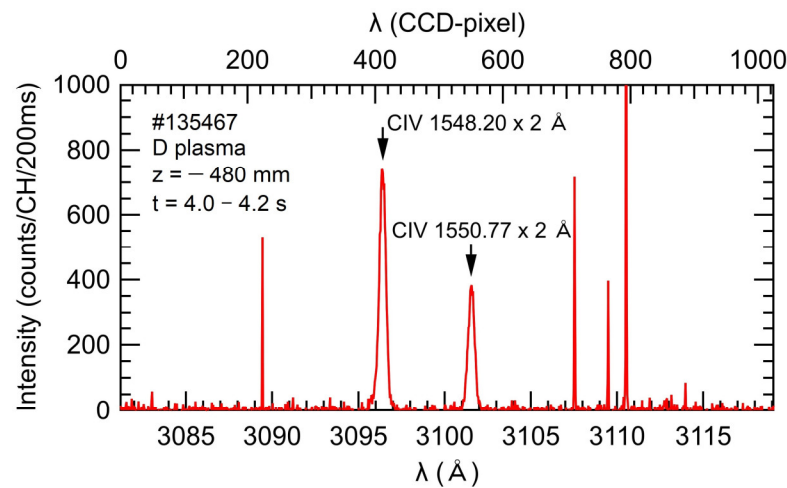


Figure 6. Wavelength spectrum of the CIV lines measured using a 3 m VUV spectrometer for a D plasma. The horizontal axis corresponds to the full wavelength range covered in a single discharge.

Figure 7a illustrates the observation range utilized for the edge profile measurement conducted with space-resolved VUV spectroscopy. Figure 7b–d present the vertical profiles at the bottom edge of the ergodic layer for CIV line intensity, ion temperature, and flow velocity, respectively. These profiles were obtained from the CIV line emission measured by VUV spectroscopy in both H plasma and D plasma. In Figure 7b–d, the horizontal axes represent the vertical position of the sightlines at $R = 3600$ mm. The data points in Figure 7b represent the emission intensity of a single line spectrum determined by the area of the peak at $\text{CIV } 1548.20 \times 2 \text{ \AA}$ from the spectrum in Figure 6. Therefore, the unit of the vertical axis is different from that in Figure 6. The flow velocity along the sightline, v_R , is determined by $v_R = c (\Delta\lambda/\lambda)$, where c is the speed of light, $\Delta\lambda$ is the Doppler shift, and λ is the wavelength of line emission. The measured flow velocity represents a projection of the flow along the observation chord, which can be approximated as the direction of the major radius of the plasma. Therefore, the variable v_R is used to indicate the measured flow value. The positive and negative signs on the horizontal axis of Figure 7d correspond to the outboard and inboard directions along the plasma major radius, respectively. In the figure, it can be observed that the emission intensity is higher in the D plasma compared to in the H plasma, which is attributed to the increased sputtering rate of carbon atoms from the divertor plates in the D plasma. The ion temperature is approximately 20–30 eV and appears to be slightly higher in the H plasma. It is worth noting that in these discharges, the electron temperature around the LCFS, as measured by Thomson scattering, is about 200 eV. The neutral hydrogen beam used for plasma heating in these discharges has an energy of 180 keV, and electron heating dominates in this energy range. Therefore, the electron temperature exceeds the ion temperature in all regions, not just at the plasma edge. The flow velocity toward the outboard direction is clearly developed, reaching its maximum value at $z = -480$ mm, which is close to the outermost region of the ergodic layer in the H plasma. This direction aligns with the friction force, in the parallel momentum balance for $R_{\text{ax}} = 3.6$ m, as calculated using three-dimensional simulation code, EMC3-EIRENE [9]. On the other hand, the maximum flow velocity in the D plasma is considerably smaller than that in the H plasma. For further discussion, it is important to note that the flow velocities observed in sightlines passing through inside the LCFS appear to have reversed signs between hydrogen and deuterium plasmas. These sightlines pass through inside and outside the torus simultaneously, which complicates the evaluation of the line integral effect. Therefore, the reason why the sign of the flow obtained by the sightlines passing through inside the LCFS is reversed between hydrogen and deuterium plasmas cannot be discussed based on this result alone. The cause may be investigated by line-integrating the results of 3D transport calculations along the sightlines used in the actual experiment to create synthetic profiles and comparing them with the experimental results.

In this paper, the discussion is limited to observations outside the LCFS, where the interpretation of the results is straightforward.

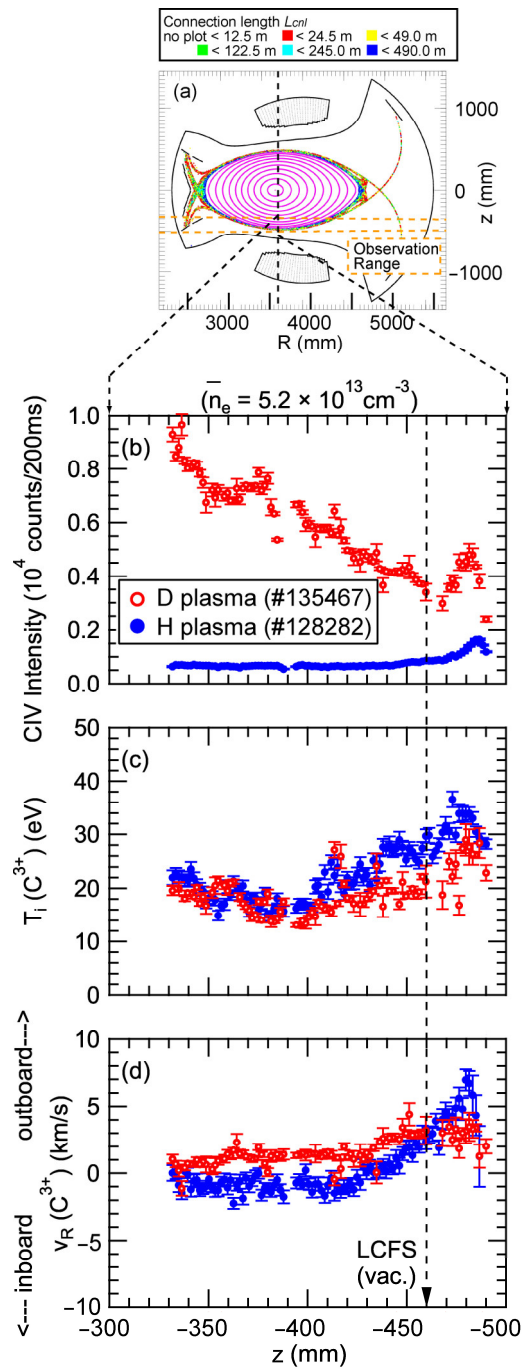


Figure 7. (a) The observation range of the 3 m VUV spectrometer at the bottom edge of the ergodic layer and the vertical profiles of (b) CIV line intensity, (c) ion temperature, and (d) flow velocity derived from the Doppler profile of the second order of CIV line emission ($1548.20 \times 2 \text{ \AA}$) for a magnetic configuration with $R_{ax} = 3.6 \text{ m}$. Open and closed circles show the results from D and H plasmas, respectively.

In Figure 8, the peak flow velocity observed at $z = -480 \text{ mm}$ is plotted against the line-averaged electron density. It can be observed that the flow velocity increases with the electron density in H plasmas, which is consistent with the simulation prediction that the friction force becomes dominant in the force balance at higher density regimes. This leads to an increase in impurity flow, potentially resulting in impurity screening. Conversely,

the flow velocity has a smaller value in the case of D plasma. Assuming a steady state and neglecting terms except for the friction force and the ion thermal force in the momentum balance, the observed parallel impurity flow in the experiment, $V_{Z//,obs}$, can be calculated using the following equation:

$$V_{Z//,obs} = \left(V_{i//} + 2.6Z^2 \frac{\tau_s}{m_Z} \frac{\partial T_i}{\partial s} \right) \cos \theta \quad (2)$$

where $V_{i//}$ is the thermal velocity of the bulk ions, Z is the charge of the impurity ion, τ_s is the impurity ion collision time, m_Z is the mass of the impurity ion, $\partial T_i / \partial s$ (< 0 in this case) is the ion temperature gradient along the magnetic field toward the divertor plate, and θ is the angle between the magnetic field line and the observation chord of the VUV spectroscopy. As n_e increases, τ_s becomes small, causing the second term on the right-hand side of Eq. (2) to become negligible. Consequently, the maximum value of $V_{Z//,obs}$ is limited by $V_{i//}$. This could explain why $V_{Z//,obs}$ saturates with increasing \bar{n}_e , as shown in Figure 8.

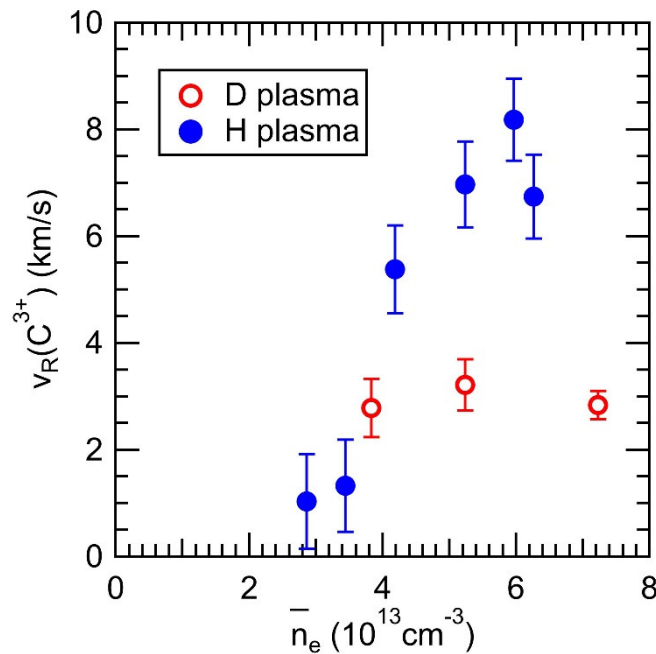


Figure 8. Observed C^{3+} flow at the bottom edge of the ergodic layer in the D and H plasmas as a function of line-averaged electron density for $R_{ax} = 3.6$ m.

In high-density operations, i.e., $\bar{n}_e \sim 5 \times 10^{13} \text{ cm}^{-3}$ on the horizontal axis in Figure 8, where the friction force is dominant, considering parameters of the plasmas at the outermost region of the ergodic layer and the spectroscopic geometry such as $T_{i,edge} = 20 \text{ eV}$, $n_{i,edge} = 2 \times 10^{13} \text{ cm}^{-3}$, and $\theta = 75^\circ$ for C^{+3} ions along the magnetic field line with the connection length of 100 m, the estimated $V_{Z//,obs}$ is 11.3 km/s for H plasmas and 8.0 km/s for D plasmas. The difference between these values for D and H plasmas is due to the $m_i^{1/2}$ dependence of $V_{i//}$ when the friction force term is dominant in the force balance. Thus, the experimental observation of smaller flow values in the D plasmas, as shown in Figure 8, qualitatively agrees with the mass dependence of $V_{i//}$. However, a more detailed comparison of edge plasma parameters between H and D plasmas is required for a quantitative discussion to explain why the carbon flow in H plasmas is approximately twice as large as that in D plasmas in high-density regions.

4. Summary

The spectroscopic diagnostics performed in the EUV and VUV wavelength ranges provided insights into the generation and transport of carbon impurities in the edge

plasmas of LHD for both H and D plasmas. The observed emission intensity of carbon CIII, CIV, CV, and CVI lines was significantly higher in the D plasma compared to in the H plasma. This suggests a larger sputtering rate of carbon materials in the D plasma, resulting in a higher quantity of carbon impurities originating from the divertor plates. To investigate the transport of carbon impurities in the ergodic layer at the edge of LHD plasma, space-resolved VUV spectroscopy was employed. It was determined that the direction of the carbon flows observed in both H and D plasmas aligned with the direction of the friction force in the parallel momentum balance acting on the impurity ions. This friction force serves as a driving force for impurity screening effects. The maximum value of the carbon flow in the D plasma was found to be smaller than that in the H plasma, indicating an isotope effect on the impurity transport. The difference in carbon impurity flow velocities between D and H plasmas can be qualitatively explained by the ion mass dependence of the bulk ion thermal velocity when the frictional force term dominates in the momentum balance.

Author Contributions: Conceptualization, T.O. and Shigeru Morita; methodology, T.O. and S.M. (Shigeru Morita); software, T.O.; validation, T.O.; formal analysis, T.O.; investigation, T.O., S.M. (Shigeru Morita), M.K., G.K., Y.K., T.K., S.M. (Suguru Masuzaki), C.S. and M.G.; resources, T.O., S.M. (Shigeru Morita), Y.K., T.K. and M.G.; data curation, T.O., Y.K., T.K. and M.G.; writing—original draft preparation, T.O.; writing—review and editing, Shigeru Morita and M.G.; visualization, T.O.; supervision, S.M. (Shigeru Morita) and M.G.; project administration, S.M. (Shigeru Morita) and M.G.; funding acquisition, T.O., S.M. (Shigeru Morita) and M.G. All authors have read and agreed to the published version of the manuscript.

Funding: This work was partially supported by JSPS KAKENHI Grant Number JP20K03896.

Data Availability Statement: Data are available on request.

Acknowledgments: The authors thank all the members of the LHD team for their cooperation with the LHD operation.

Conflicts of Interest: The authors declare no conflict of interest.

References

1. Stangeby, P.C.; McCracken, G.M. Plasma boundary phenomena in tokamaks *Nucl. Fusion* **1990**, *30*, 1225–1379. <https://doi.org/10.1088/0029-5515/30/7/005>.
2. Evans, T.E.; Moyer, R.A.; Thomas, P.R.; Watkins, J.G.; Osborne, T.H.; Boedo, J.A.; Doyle, E.J.; Fenstermacher, M.E.; Finken, K.H.; Groebner, R.J.; et al. Suppression of Large Edge-Localized Modes in High-Confinement DIII-D Plasmas with a Stochastic Magnetic Boundary. *Phys. Rev. Lett.* **2004**, *92*, 235003. <https://doi.org/10.1103/physrevlett.92.235003>.
3. Kobayashi, M.; Masuzaki, S.; Yamada, I.; Tamura, N.; Feng, Y.; Sato, K.; Goto, M.; Narushima, Y.; Akiyama, T.; Miyazawa, J.; et al. Detachment stabilization with $n/m = 1/1$ resonant magnetic perturbation field applied to the stochastic magnetic boundary of the Large Helical Device. *Phys. Plasmas* **2010**, *17*, 056111. <https://doi.org/10.1063/1.3368681>.
4. Morisaki, T.; Narihara, K.; Masuzaki, S.; Morita, S.; Goto, M.; Komori, A.; Ohyabu, N.; Motojima, O.; Matsuoka, K. Ergodic edge region of large helical device. *J. Nucl. Mater.* **2003**, *313–316*, 548–552. [https://doi.org/10.1016/s0022-3115\(02\)01467-8](https://doi.org/10.1016/s0022-3115(02)01467-8).
5. Chowdhuri, M.B.; Morita, S.; Kobayashi, M.; Goto, M.; Zhou, H.; Masuzaki, S.; Morisaki, T.; Narihara, K.; Yamada, I.; Feng, Y. Experimental study of impurity screening in the edge ergodic layer of the Large Helical Device using carbon emissions of CIII to CVI. *Phys. Plasmas* **2009**, *16*, 062502. <https://doi.org/10.1063/1.3103784>.
6. Morita, S.; Dong, C.; Kobayashi, M.; Goto, M.; Huang, X.; Murakami, I.; Oishi, T.; Wang, E.; Ashikawa, N.; Fujii, K.; et al. Effective screening of iron impurities in the ergodic layer of the Large Helical Device with a metallic first wall. *Nucl. Fusion* **2013**, *53*, 093017. <https://doi.org/10.1088/0029-5515/53/9/093017>.
7. Kobayashi, M.; Morita, S.; Dong, C.; Cui, Z.; Pan, Y.; Gao, Y.; Zhou, H.; Feng, Y.; Masuzaki, S.; Goto, M.; et al. Edge impurity transport study in the stochastic layer of LHD and the scrape-off layer of HL-2A. *Nucl. Fusion* **2013**, *53*, 033011. <https://doi.org/10.1088/0029-5515/53/3/033011>.
8. Stangeby, P.C. *The Plasma Boundary of Magnetic Fusion Devices*; 1st ed.; Institute of Physics Publishing: Bristol, UK, 2000; pp. 296–323. <https://doi.org/10.1201/9780367801489>.
9. Oishi, T.; Morita, S.; Dai, S.; Kobayashi, M.; Kawamura, G.; Huang, X.; Zhang, H.; Liu, Y.; Goto, M.; The LHD Experiment Group. Observation of carbon impurity flow in the edge stochastic magnetic field layer of Large Helical Device and its impact on the edge impurity control. *Nucl. Fusion* **2018**, *58*, 016040. <https://doi.org/10.1088/1741-4326/aa8f63>.

10. Dai, S.; Oishi, T.; Kawamura, G.; Kobayashi, M.; Morita, S.; Feng, Y.; Wang, D. Three-dimensional simulations of edge impurity flow obtained by the vacuum ultraviolet emission diagnostics in the Large Helical Device with EMC3-EIRENE. *Nucl. Fusion* **2018**, *58*, 096024. <https://doi.org/10.1088/1741-4326/aace69>.
11. Dai, S.; Kobayashi, M.; Kawamura, G.; Morita, S.; Zhang, H.; Oishi, T.; Feng, Y.; Wang, D.; Suzuki, Y. EMC3-EIRENE modelling of edge impurity transport in the stochastic layer of the large helical device compared with extreme ultraviolet emission measurements. *Nucl. Fusion* **2016**, *56*, 066005. <https://doi.org/10.1088/0029-5515/56/6/066005>.
12. Takeiri, Y.; Morisaki, T.; Osakabe, M.; Yokoyama, M.; Sakakibara, S.; Takahashi, H.; Nakamura, Y.; Oishi, T.; Motojima, G.; Murakami, S.; et al. Extension of the operational regime of the LHD towards a deuterium experiment. *Nucl. Fusion* **2017**, *57*, 102023. <https://doi.org/10.1088/1741-4326/aa7fc2>.
13. Osakabe, M.; Takahashi, H.; Yamada, H.; Tanaka, K.; Kobayashi, T.; Ida, K.; Ohdachi, S.; Varela, J.; Ogawa, K.; Kobayashi, M.; et al. Recent results from deuterium experiments on the large helical device and their contribution to fusion reactor development. *Nucl. Fusion* **2022**, *62*, 042019. <https://doi.org/10.1088/1741-4326/ac3cda>.
14. Chowdhuri, M.B.; Morita, S.; Goto, M. Characteristics of an absolutely calibrated flat-field extreme ultraviolet spectrometer in the 10–130 Å range for fusion plasma diagnostics. *Appl. Opt.* **2008**, *47*, 135–146. <https://doi.org/10.1364/ao.47.000135>.
15. Chowdhuri, M.B.; Morita, S.; Goto, M.; Nishimura, H.; Nagai, K.; Fujioka, S. Spectroscopic comparison between 1200 grooves/mm ruled and holographic gratings of a flat-field spectrometer and its absolute sensitivity calibration using bremsstrahlung continuum. *Rev. Sci. Instrum.* **2007**, *78*, 023501. <https://doi.org/10.1063/1.2437742>.
16. Oishi, T.; Morita, S.; Huang, X.; Zhang, H.; Goto, M.; the LHD Experiment Group. Line Spectrum of Tungsten Ions at Low Ionization Stages in Large Helical Device in Wavelength Range of 300–2400 Å Measured Using 20 cm Normal Incidence VUV Spectrometers. *Plasma Fusion Res.* **2015**, *10*, 3402031. <https://doi.org/10.1585/pfr.10.3402031>.
17. Oishi, T.; Morita, S.; Dong, C.; Wang, E.; Huang, X.; Goto, M.; LHD Experiment Group Space-resolved 3 m normal incidence spectrometer for edge impurity diagnostics in the large helical device. *Appl. Opt.* **2014**, *53*, 6900–6912. <https://doi.org/10.1364/ao.53.006900>.
18. Oishi, T.; Morita, S.; Kobayashi, M.; Mukai, K.; Kawamura, G.; Masuzaki, S.; Hayashi, Y.; Suzuki, C.; Kawamoto, Y.; Goto, M.; et al. EUV and VUV Spectra of NeIII-NeX Line Emissions Observed in the Impurity Gas-Puffing Experiments of the Large Helical Device. *Plasma Fusion Res.* **2021**, *16*, 2402006. <https://doi.org/10.1585/pfr.16.2402006>.
19. Oishi, T.; Ashikawa, N.; Nespoli, F.; Masuzaki, S.; Shoji, M.; Gilson, E.; Lunsford, R.; Morita, S.; Goto, M.; Kawamoto, Y.; et al. Line identification of boron and nitrogen emissions in EUV and VUV wavelength ranges in the impurity powder dropping experiments of LHD and its application to spectroscopic diagnostics. *Plasma Sci. Technol.* **2021**, *23*, 084002. <https://doi.org/10.1088/2058-6272/abfd88>.
20. Oishi, T.; Morita, S.; Kato, D.; Murakami, I.; Sakaue, H.A.; Kawamoto, Y.; Kawate, T.; Goto, M. Simultaneous Observation of Tungsten Spectra of W^0 to W^{46+} Ions in Visible, VUV and EUV Wavelength Ranges in the Large Helical Device. *Atoms* **2021**, *9*, 69. <https://doi.org/10.3390/atoms9030069>.
21. Katai, R.; Morita, S.; Goto, M. High-Resolution VUV Spectra of Carbon, Neon and Argon in a Wavelength Range of 250 to 2300 Å for Plasma Diagnostics Observed with a 3 m Normal Incidence Spectrometer in LHD. *Plasma Fusion Res.* **2007**, *2*, 14. <https://doi.org/10.1585/pfr.2.014>.
22. Oishi, T.; Morita, S.; Huang, X.; Zhang, H.; Goto, M.; the LHD Experiment Group Observation of W IV–W VII line emissions in wavelength range of 495–1475 Å in the large helical device. *Phys. Scr.* **2016**, *91*, 025602. <https://doi.org/10.1088/0031-8949/91/2/025602>.
23. Kramida, A.; Ralchenko, Y.; Reader, J.; NIST ASD Team. *NIST Atomic Spectra Database*, (ver. 5.10); National Institute of Standards and Technology: Gaithersburg, MD, USA, 2022. Available online: <https://physics.nist.gov/asd> (accessed on 15 March 2023).
24. Nishimura, K.; Ashikawa, N.; Sagara, A.; Noda, N.; Kawahata, K.; Morita, S.; Peterson, B.J.; Sakakibara, S.; Takeiri, Y.; Tanaka, K.; et al. Effects of Boronization in LHD. *J. Plasma Fusion Res.* **2003**, *79*, 1216–1217. <https://doi.org/10.1585/jspf.79.1216>.
25. Morita, S.; Goto, M. X-ray crystal spectrometer with a charge-coupled-device detector for ion temperature measurements in the Large Helical Device. *Rev. Sci. Instrum.* **2003**, *74*, 2375–2387. <https://doi.org/10.1063/1.1556942>.
26. Vietzke, E. Isotope Dependence of the Chemical Erosion of Graphite by Hydrogen/Deuterium Implantation. *J. Nucl. Sci. Technol.* **2002**, *39*, 363–366. <https://doi.org/10.1080/18811248.2002.9715204>.
27. Liu, Y.; Morita, S.; Oishi, T.; Goto, M. Effect of neutron and γ -ray on charge-coupled device for vacuum/extreme ultraviolet spectroscopy in deuterium discharges of large helical device. *Rev. Sci. Instrum.* **2018**, *89*, 10I109. <https://doi.org/10.1063/1.5037233>.

Disclaimer/Publisher’s Note: The statements, opinions and data contained in all publications are solely those of the individual author(s) and contributor(s) and not of MDPI and/or the editor(s). MDPI and/or the editor(s) disclaim responsibility for any injury to people or property resulting from any ideas, methods, instructions or products referred to in the content.